

Supporting Information

Nickel Confined in the Interlayer Region of Birnessite: an Active Electrocatalyst for Water Oxidation

*Akila C. Thenuwara, Elizabeth B. Cerkez, Samantha L. Shumlas, Nuwan H. Attanayake, Ian G. McKendry, Laszlo Frazer, Eric Borguet, Qing Kang, Richard C. Remsing, Michael L. Klein, Michael J. Zdilla, and Daniel R. Strongin**

anie_201601935_sm_miscellaneous_information.pdf

Table of Contents	Page
Experimental section	3
Molecular Dynamics Simulations	5
Electrochemical characterization and catalytic parameter calculations	8
List of Tables	
Table S1. Parameters for fitted EIS spectra	21
Table S2. Comparison of catalytic performance	28
List of Figures	
Figure S1. SEM of Ni ²⁺ /birnessite	10
Figure S2. STEM and EDS of Ni ²⁺ /birnessite	11
Figure S3. XRD for birnessite exposed to hydrazine and Mn ₃ O ₄	12
Figure S4. Raman spectra	13
Figure S5. XPS of Ni ²⁺ /birnessite	14
Figure S6. XPS spectrum of O 1s for birnessite	15
Figure S7. MD simulation radial distribution functions and snapshot	16
Figure S8. MD simulation radial distribution functions and snapshot	17
Figure S9. MD simulation for hydrazine and Ni ²⁺	18
Figure S10. Nyquist plot obtained from EIS measurement	19
Figure S11. Equivalent circuit used to obtain charge transfer resistance	20
Figure S12. Oxygen detection by Gas Chromatography (GC)	22
Figure S13. Chronopotentiometry measurement	23
Figure S14. β-Nickel hydroxide XRD	24

Figure S15. β -Nickel hydroxide TEM	25
Figure S16. Raman and TEM data after catalyst cycling	26
Figure S17. XPS after catalyst cycling	27
Figure S18. Capacitance measurement to estimate ECSA	29
Figure S19. Polarization curves obtained after cycling of Ni^{2+} /Birnessite	30
Figure S20. MD Microscopic picture of the Ni^{2+} ion intercalated birnessite	31
Figure S21. Snapshots of water and ions in Ni^{2+} /birnessite	32
References	33

Experimental

Materials and Methods

All chemical reagents used in this study were purchased from commercial vendors and used without further purification. X-ray diffraction (XRD) data were acquired on a Bruker Kappa APEX II DUO diffractometer using Mo K α radiation from a sealed molybdenum tube with a TRIUMPH monochromator. X-ray photoelectron spectroscopy (XPS) of the catalyst powders was conducted with a Thermo Scientific K-alpha+ at the University of Delaware. XPS analysis of the catalyst ink (pre and post catalysis) was carried out using a VG Scientific 100 mm hemispherical analyzer and a Physical Electronics Mg K α X-ray source operating at 280W. Transmission electron microscopy (TEM) images were obtained using a JEOL JEM-1400 microscope operating at 120 kV. Scanning electron microscopy (SEM) images were obtained using a FEI Quanta 450 FEG-SEM microscope operating at 30 kV. Energy dispersive spectroscopy (EDS) analysis was performed with an Oxford systems nano-analysis EDS system, using Aztec 2.1 as the analyzing software. Elemental analysis was performed using a Thermo Scientific iCAP 7000 Series Inductively Coupled Plasma with an Optical Emission Spectrometer (ICP-OES). Raman measurements were performed using a Horiba Labram HR800 Evolution confocal Raman spectrometer with 532 nm excitation and a 100X objective. The resolution of the Raman spectrometer was $\sim 3\text{ cm}^{-1}$. The excitation laser intensity was maintained below the sample optical damage threshold. All samples were pressed into pellets by applying 5 tons for 3 minutes to obtain a smooth surface for Raman analysis.

Synthesis of potassium birnessite. Hydrochloric acid (4 M, 50.0 mL) was added drop wise via a syringe pump at 1 mL/min to a heated and stirred (80 °C , 360 rpm) solution of potassium permanganate (0.200 M, 250 mL) in a 400 mL beaker. Heating continued at 80 °C for an

additional 0.5 h after addition was completed. The resulting 300 mL solution was then covered to prevent excessive evaporation overnight and aged for 15 h at 50 °C. Finally the resulting suspension was washed several times with distilled water and dried under room temperature.

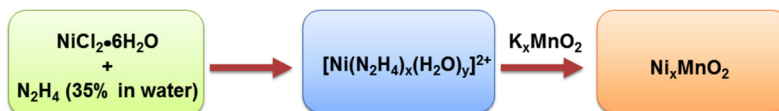
Nickel hydroxide synthesis. The beta phased Ni(OH)₂ was synthesized by a modified microwave-assisted method as described below. Nickel (II) nitrate hexahydrate and urea were dissolved in molar ratio of 1:4 in 30 mL deionized water, and the resulting solution was treated under microwave irradiation in a standard microwave at 900 W for several minutes. Next, the resulting green colloidal suspension was cooled down to room temperature and retrieved by centrifugation. Finally, the products were washed several times with distilled water and absolute ethanol and dried in an oven at 60 °C for 12 h.

Synthesis of nickel intercalated birnessite. Nickel intercalated birnessite (referred to as Ni²⁺/birnessite hereafter) catalyst was prepared via a wet chemical ion exchange reaction. The nickel precursor solution was prepared by adding 0.100 g (0.422 mmol) of nickel chloride hexahydrate (NiCl₂•6H₂O) to 20 mL of deionized water (18.3 MΩ cm). Next, stoichiometric amounts (19 μL, 0.204 mmol) of hydrazine solution (35 wt. % in H₂O) were added to the nickel precursor solution. A noticeable color change from green to pale blue was observed after the addition of hydrazine, which is an indication of the formation of the nickel-hydrazine complex (Equation S1).¹ After stirring for 5 mins, 0.100 g of synthetic birnessite was added to the nickel-hydrazine complex containing solution and the suspension was stirred for 10 mins. Finally, the solution was vacuum filtered and the residue washed with excess deionized water. In order to examine the effect of reaction time as well as the effect of starting nickel precursor amount, a

series of Ni²⁺/birnessite samples were synthesized, and the exposure time of birnessite to the nickel-hydrazine complex was varied from 10 to 30 min (Scheme S1).



Scheme S1. Synthesis route for Ni²⁺/birnessite



Molecular Dynamics Simulations

To characterize the free energy landscape underlying electron transfer (ET) involving cations in the interlayer region or in bulk, we follow previous work.² In particular, we use GROMACS³ with the CLAYFF⁴ force field to perform molecular dynamics (MD) simulations with varying charge states of a single ion. This enables umbrella sampling of the so-called energy gap,

$$\Delta E = H_1 - H_0, \quad (\text{S2})$$

where, H_1 and H_0 are the Hamiltonians of the oxidized and reduced states of the cation, respectively. The energy gap ΔE has been shown to be a good order parameter for describing ET.⁵⁻⁷ Note that unlike the previous work,² we only consider the portion of the Hamiltonians regarding the cation undergoing ET, and, in the case of the birnessite system, we omit the energetic changes involving a manganese atom undergoing a concomitant reduction in charge. This allows us to better compare the free energetics in bulk and in birnessite. MD simulations involving nickel ions were performed using the CM model of Merz and coworkers.⁸ This model captures the salient features regarding hydration of Ni²⁺ ions, including the octahedral

coordination structure. We additionally used this model to study the solvation structure of Ni^{2+} in hydrazine and water/hydrazine mixtures.

Solvation Structure of Ni^{2+}

Here we compare the solvation structure of the Ni^{2+} ion in water and in hydrazine from molecular dynamics (MD) simulations. Water and Ni^{2+} are modeled with the SPC/E⁹ and Merz CM potentials,^{4,10} respectively. Hydrazine is modeled with the potential of Maginn and coworkers.¹¹ To obtain the solvation structure of Ni^{2+} in water and hydrazine, we simulated a single ion in 4142 molecules of SPC/E water and 343 molecules of hydrazine, with a neutralizing uniform background charge density to maintain the neutrality of the system. To study Ni^{2+} solvation in a water/hydrazine mixture, we simulated a system of 686 nickel ions, 343 hydrazine molecules (2:1 nickel: hydrazine), 31744 water molecules, and 1372 chloride ions to maintain neutrality. Simulations were performed for 5 ns at a constant temperature¹² and pressure¹³ of 300 K and 1 bar, respectively, after equilibrating the system at very high temperatures (1000 K) at constant volume to ensure adequate mixing.

Figure S10a shows the radial distribution function $g(r)$ and corresponding coordination number $CN(r)$ for water oxygen atoms surrounding a single Ni^{2+} ion. The first hydration shell, corresponding to the first peak in $g(r)$, is highly ordered and consists of 6 water molecules tightly bound to the ion. This corresponds to the complex $[\text{Ni}(\text{H}_2\text{O})_6]^{2+}$. The water molecules are organized octahedrally around the nickel ion, as shown in snapshot in Figure S10b.

In contrast, only 4 hydrazine molecules are found in the first solvation shell of Ni^{2+} , as indicated by the $g(r)$ between the center of mass of hydrazine molecules and the nickel ion and the corresponding coordination number shown in Figure S11a. As illustrated by the snapshot in Figure S11b, the nitrogen atoms of two hydrazine molecules in the coordination shell occupy

octahedral sites, while the remaining two octahedral sites are occupied by the remaining two hydrazine molecules, mostly by the midpoint between the two nitrogen atoms, forming the complex $[\text{Ni}(\text{N}_2\text{H}_4)_4]^{2+}$ in solution. Similar results for both water and hydrazine solvation are also obtained using a multi-site representation of Ni^{2+} with explicit octahedral site¹⁴.

The above results demonstrate that both water and hydrazine bind octahedrally to Ni^{2+} . Thus, in a mixture, water and hydrazine will compete for the six octahedral binding sites that are available, and we expect a distribution of coordination structure compositions in such mixtures. The probability distribution of coordination numbers around nickel ions in the simulations water/hydrazine mixture is shown in Figure S12a. Note that the hydrazine coordination number is defined here as the number of nitrogen atoms in the coordination shell in order to better examine the number of octahedral sites occupied around each ion. Additionally, Cl^- ions are also found in the solvation shell of Ni^{2+} , such that water and hydrazine are not the only coordinating species, but our main concern here are mixed water/hydrazine coordination structures.

The water distribution is bimodal, with peaks at 2 and 5 atoms. The hydrazine distribution is maximal at zero, but has non-zero probability at 1, 2, and 4 nitrogen atoms surrounding Ni^{2+} , while 2 being the most probable non-zero number of coordinated nitrogen atoms. This means, as one may expect from the composition of the solution (2:1 Ni^{2+} :hydrazine), the cations are largely coordinated by one hydrazine, if at all. These solvation structures are still octahedrally coordinated, but are now composed of both water and hydrazine molecules, see Figure S12b for a representative snapshot.

The observed coordination structures may be important for understanding how Ni^{2+} ions are “shuttled” into the birnessite interlayer. The one or two hydrazine molecules in the coordination shell may dissociate from the nickel complex by undergoing a chemical reaction

with the birnessite edges or through other means (like thermal fluctuations) when close to birnessite. Once these hydrazine molecules, which do not penetrate the interlayer, are removed from the coordination shell, the under coordinated Ni^{2+} ion could be driven into the negatively charged interlayer region through electrostatic interactions. However, further studies are needed to uncover the details of this mechanism.

Electrochemical Characterization

Electrocatalytic studies were carried out in an alkaline medium (1 M KOH) using a CHI 660E potentiostat operating in a standard three-electrode configuration at ambient temperature (22 ± 2 °C). All the potentials were measured with respect to a standard calomel reference electrode (CH instruments) and Pt wire was used as the counter electrode. The working electrode was prepared by drop casting 5 μL of catalyst ink suspension on a 3 mm diameter glassy carbon electrode (loading 0.28 mg/cm^2). The ink solution was prepared by adding 4 mg of catalyst and 4 mg of carbon (VulcanXC-72), which was dispersed in 1 mL isopropanol and 35 μL of Nafion solution (5% in alcohol, Ion Power Inc.). The resulting mixture was sonicated for at least 1 hour to form a catalyst ink. All the polarization curves were recorded at 10 mV/s scan rate. For all the catalysts tested here, polarization curves were replicated 5 times. The overpotential (at a current density of 10 mA/cm^2) and Tafel slopes reported are based on an analysis of these data.

Catalytic parameter calculations

The turnover frequency (TOF) value is calculated from the equation:

$$TOF = \frac{JA}{4Fn}$$

where, J is the measured current density (mA cm^{-2}) at $\eta = 0.40$ V, A is the geometric area of the electrode, n is the number of moles catalyst loading, and F is the Faraday constant (96500 C mol^{-1}).

The mass activity was calculated from following equation:

$$\text{mass activity} = \frac{J}{m}$$

The mass activity (A g^{-1}) was calculated on the basis of the catalyst loading $m = 0.28 \text{ mg cm}^{-2}$ and the measured current density j (mA cm^{-2}) at $\eta = 0.40$ V.

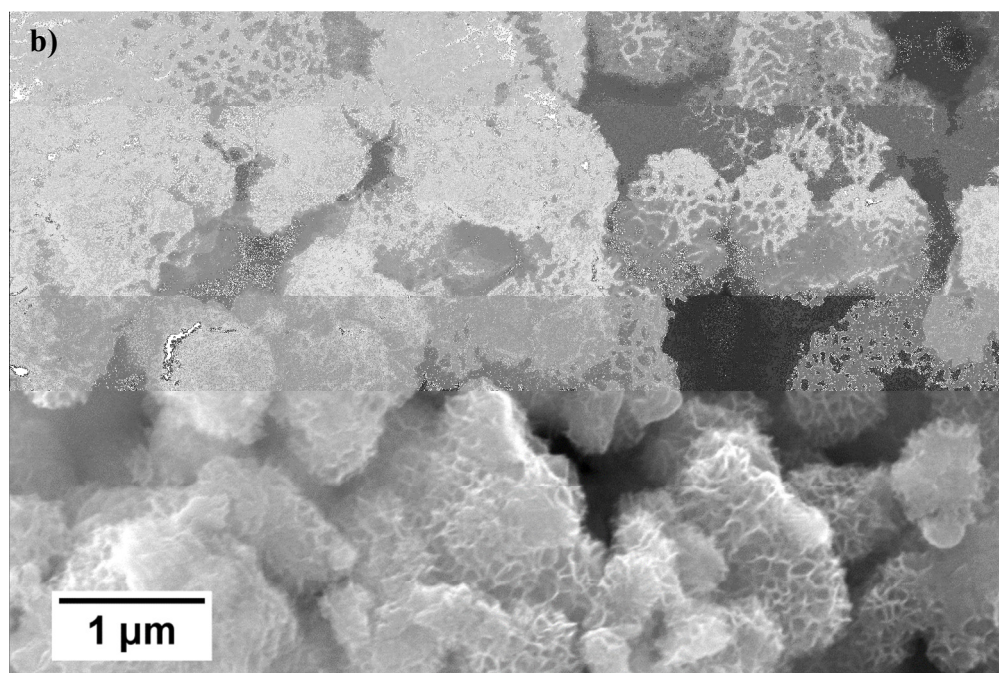
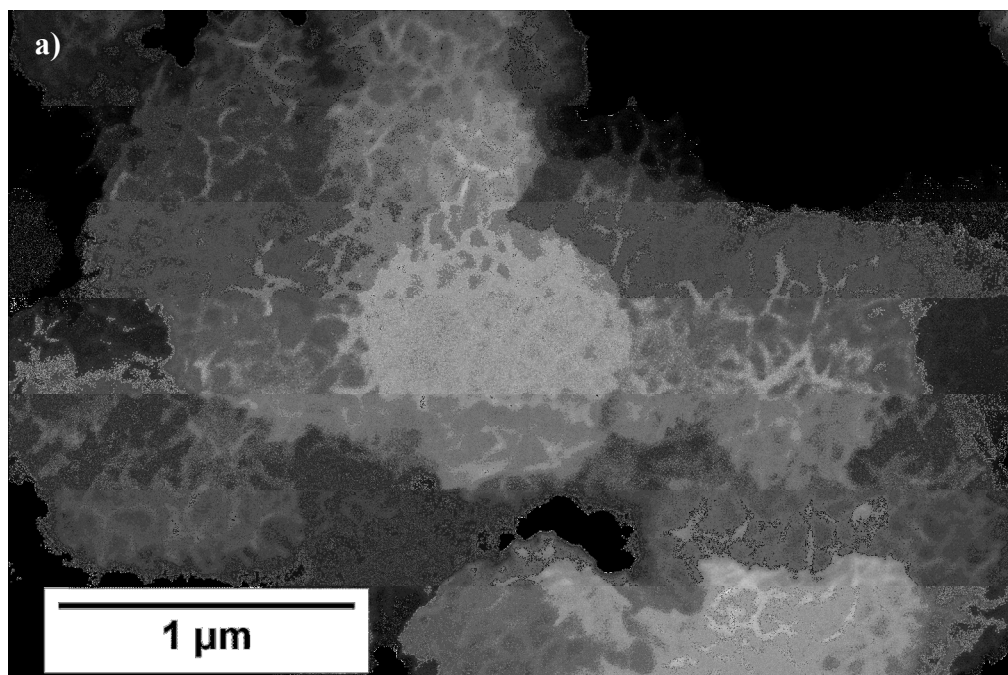


Figure S1. Scanning Electron Microscopy images of Ni²⁺/birnessite: a) Ni²⁺/birnessite (Ni 6.6%) and b) Ni²⁺/birnessite (Ni 7.7%).

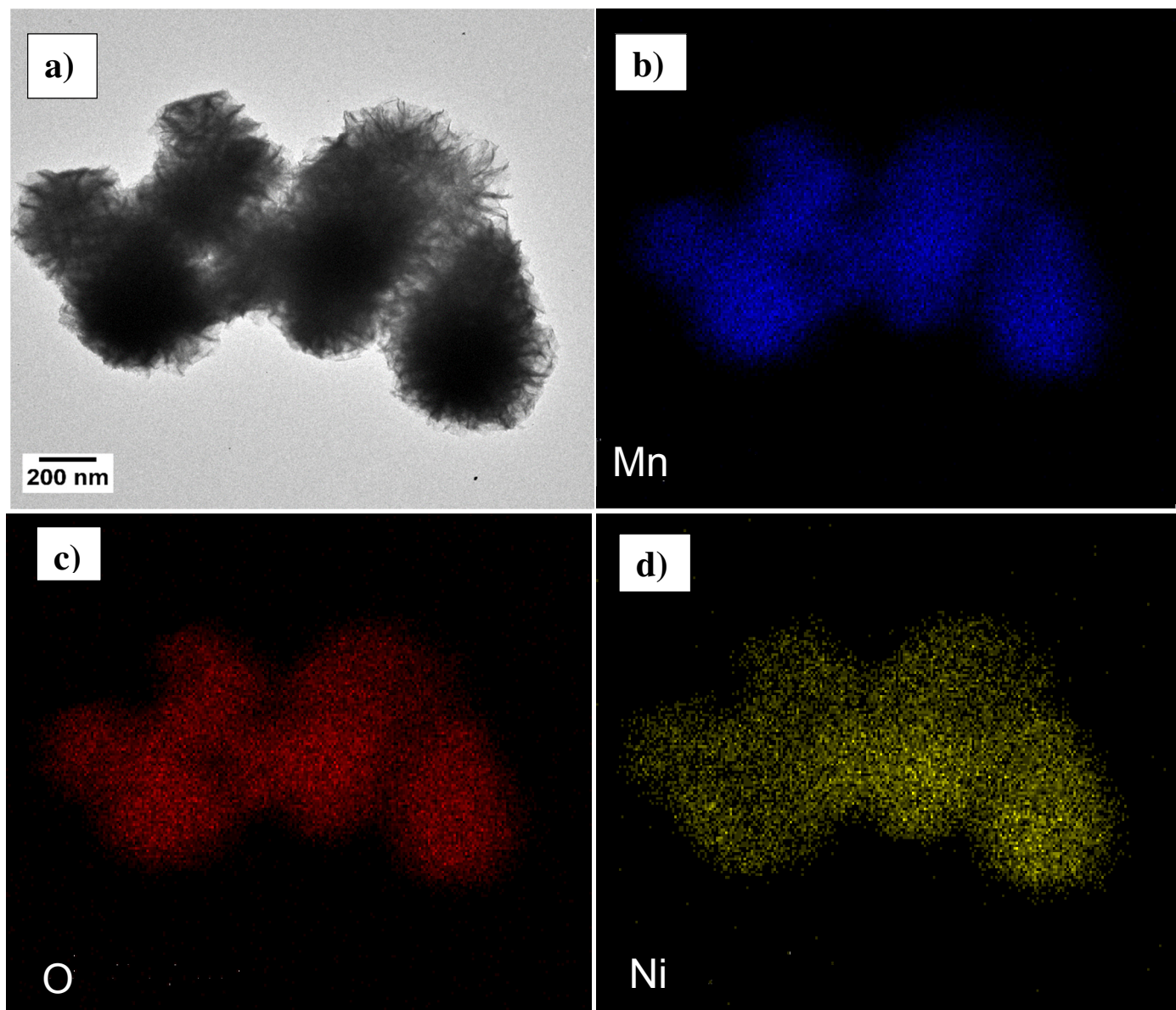


Figure S2. a) STEM image of Ni^{2+} /Birnessite, b), c) and d) are EDS elemental maps of Mn, O and Ni respectively. These particular results suggest a homogeneous distribution of Ni in the birnessite structure.

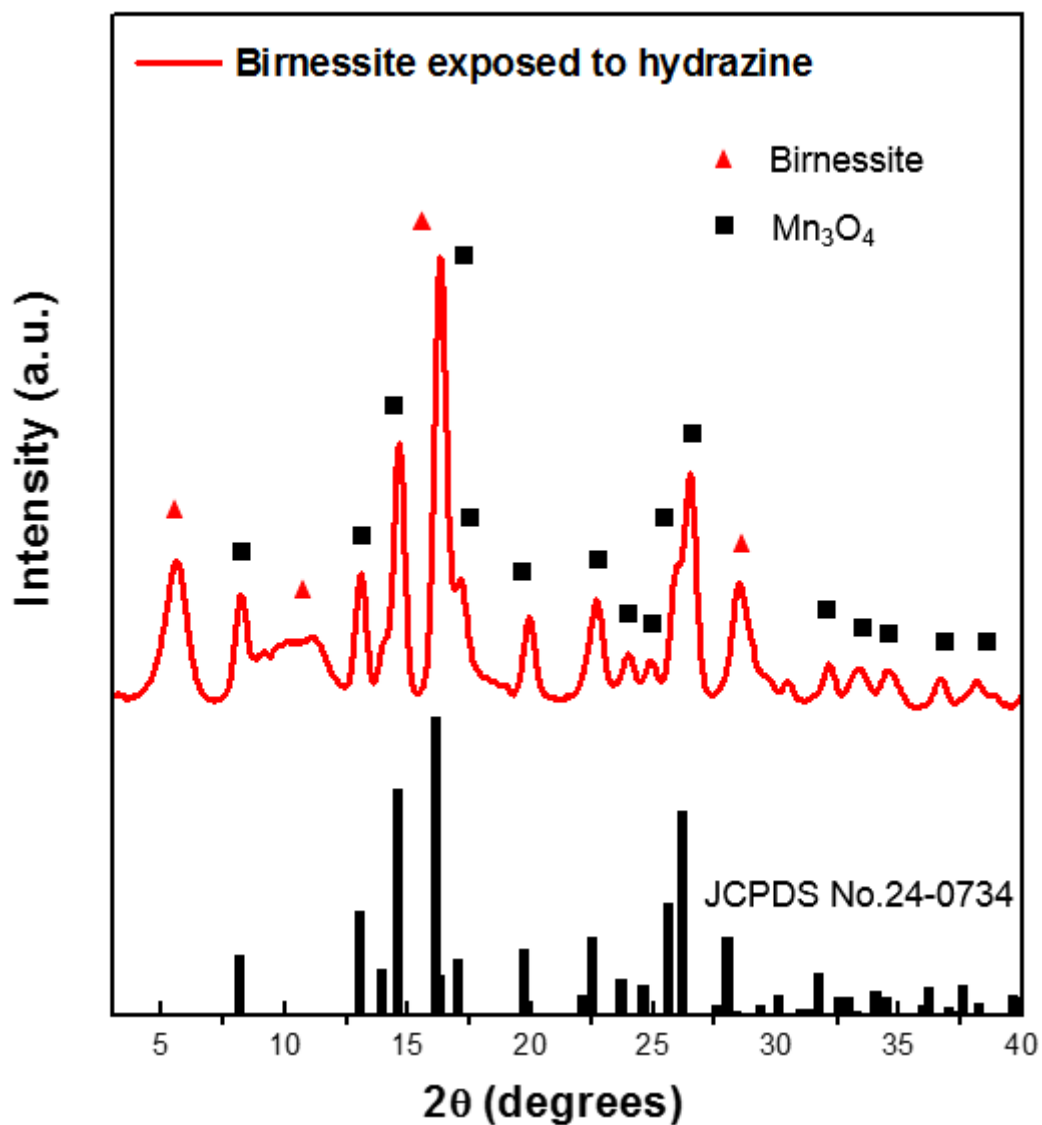


Figure S3. Experimental XRD pattern for birnessite exposed to hydrazine with the standard diffraction of tetragonal Mn_3O_4 (JCPDS no. 24-0734). Results suggest that birnessite transforms into Mn_3O_4 when exposed to hydrazine.

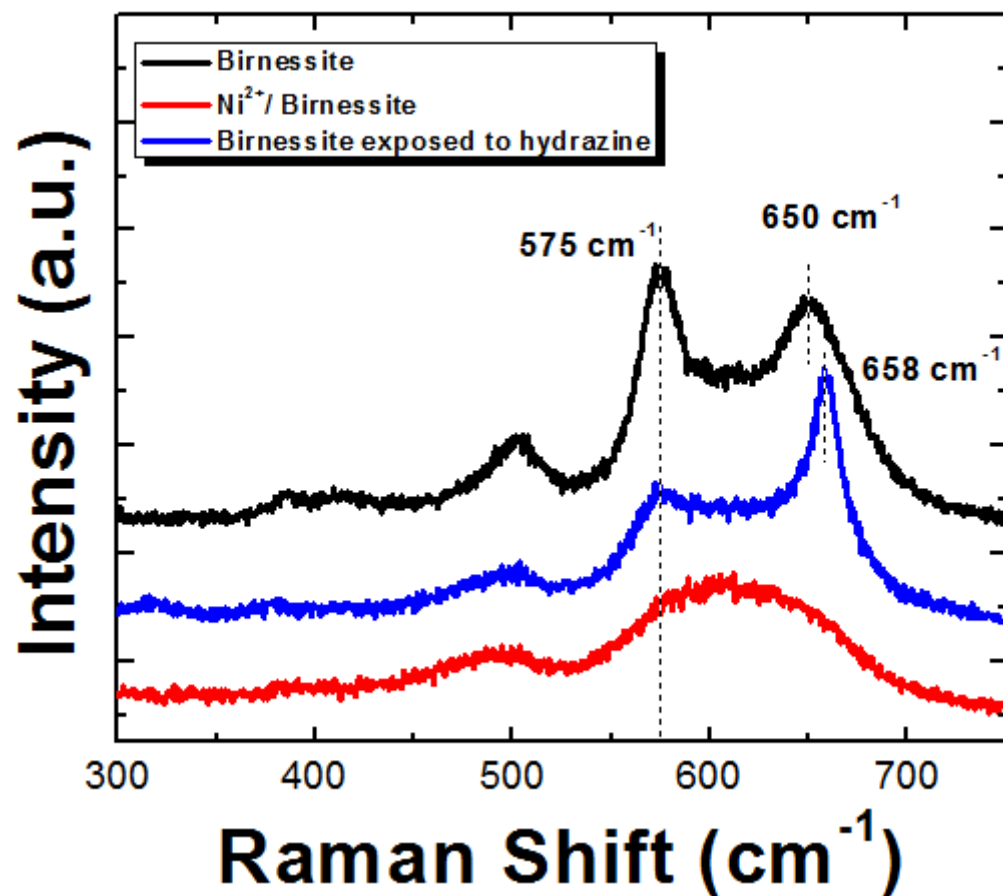


Figure S4. Raman spectra of birnessite, birnessite exposed to hydrazine and Ni²⁺/birnessite. The Raman peaks are broadened by the disorder in the birnessite lattice induced by the presence of Ni²⁺ in the interlayer region.

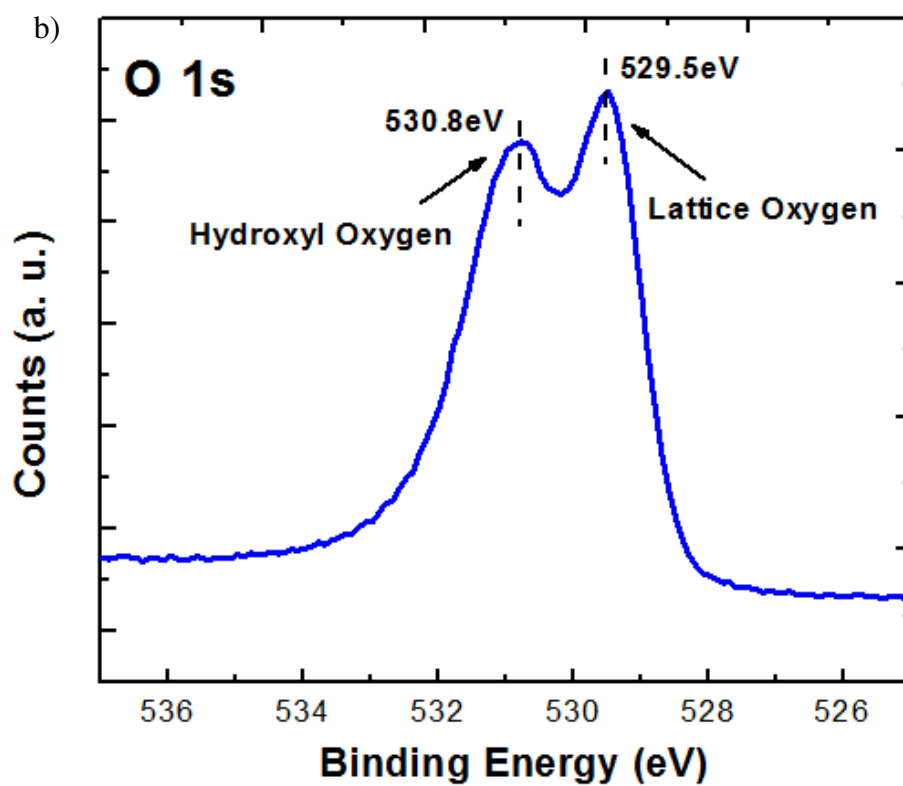
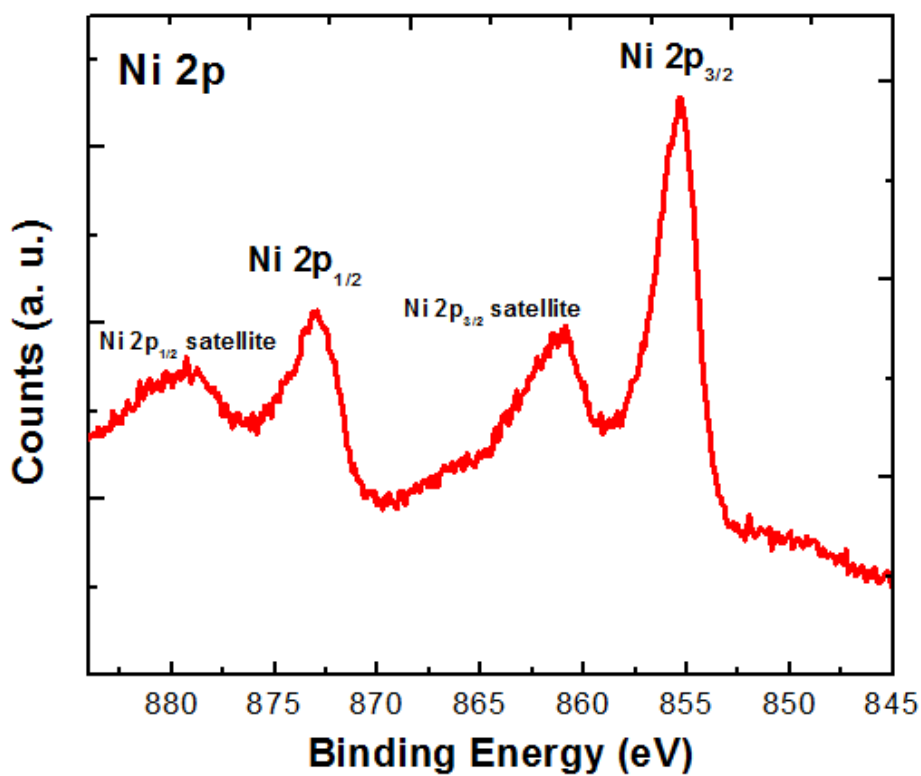


Figure S5. XPS of Ni^{2+/}birnessite: a) Ni 2p region b) O 1s region. The spectra suggest that nickel in the interlayer has nickel hydroxide character.

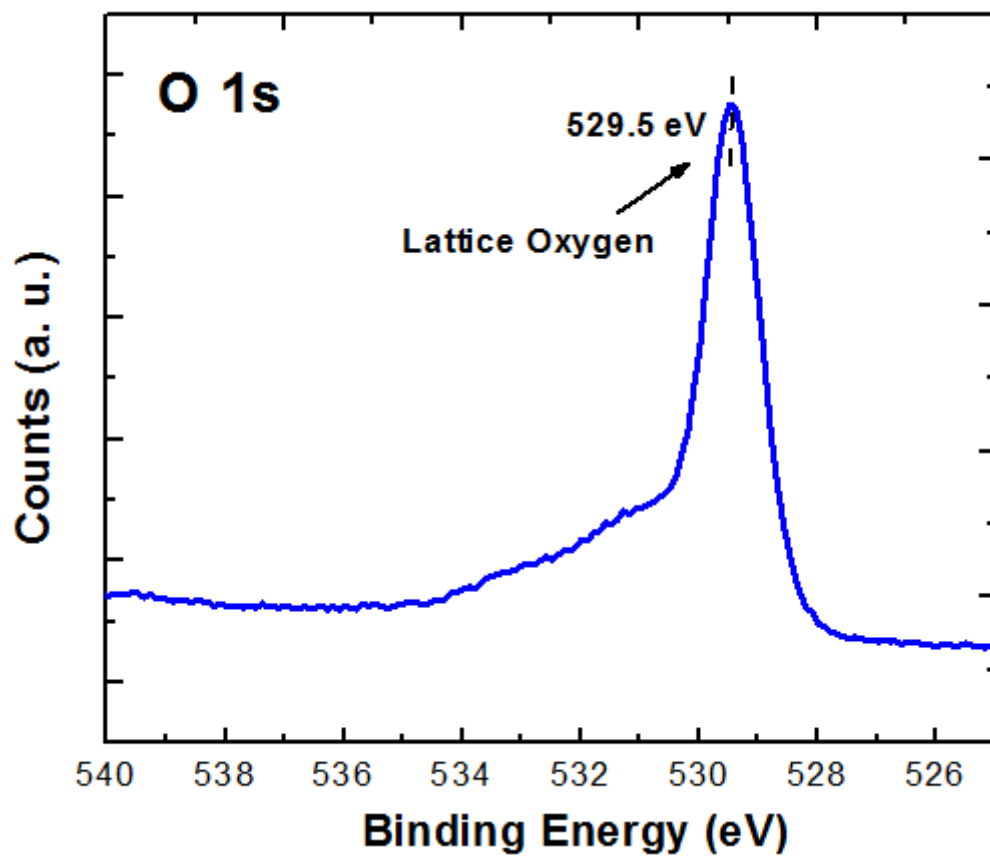


Figure S6. XPS spectrum of O 1s core level spectra for birnessite indicating the presence of the lattice oxygen peak and the absence of a hydroxide O 1s contribution.

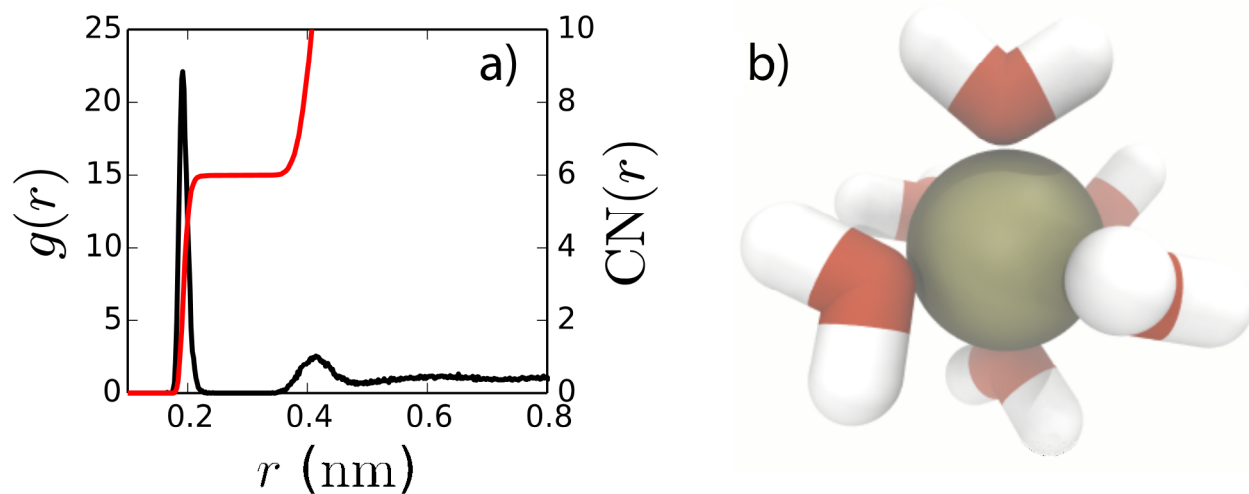


Figure S7. a) Radial distribution function ($g(r)$, black) and coordination number ($CN(r)$, red) for water oxygen atoms around a nickel ion. b) Snapshot of a typical Ni^{2+} hydration shell, highlighting the octahedral arrangement of water molecules around the ion. Water oxygen and hydrogen atoms are colored red and white, respectively, while Ni^{2+} is colored tan.

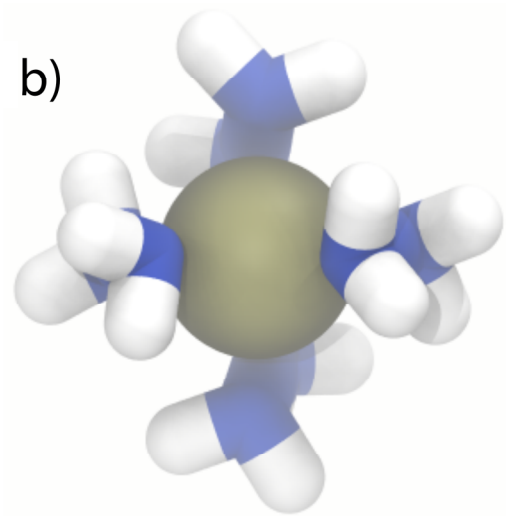
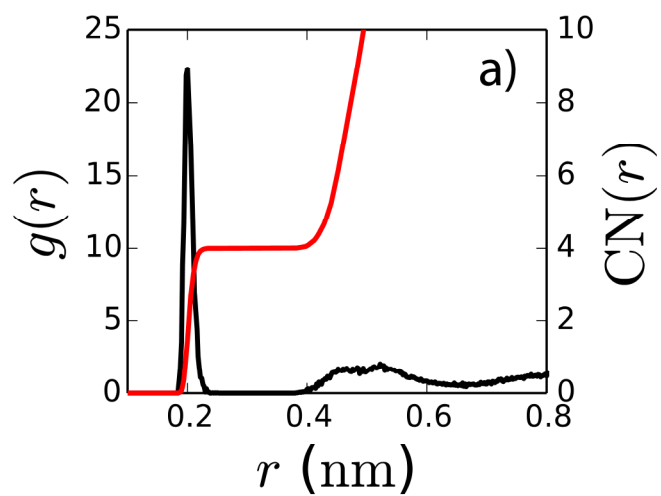


Figure S8. a) Radial distribution function ($g(r)$, black) and coordination number ($CN(r)$, red) for the center of mass of hydrazine molecules around a nickel ion. b) Snapshot of a typical Ni^{2+} coordination shell, highlighting the octahedral-like arrangement of hydrazine around the ion. Hydrazine nitrogen and hydrogen atoms are colored blue and white, respectively, while Ni^{2+} is colored tan.

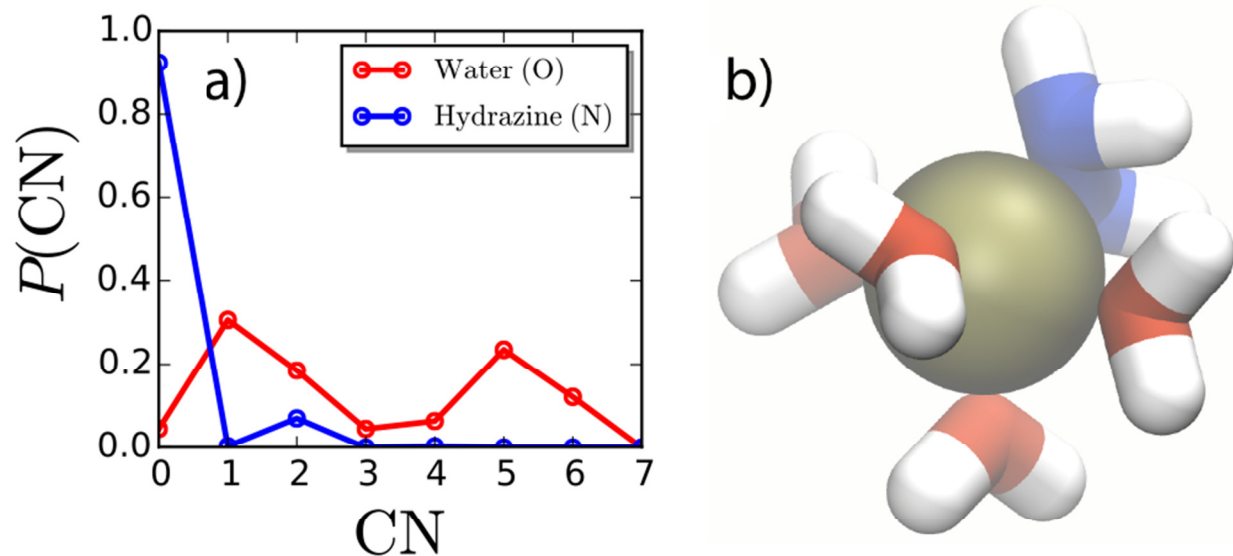


Figure S9. a) Probability of observing the coordination number (CN) of water oxygen atoms (red) and hydrazine nitrogen atoms (blue) around a Ni^{2+} ion. b) Snapshot of a typical Ni^{2+} coordination shell involving 4 water molecules and 1 hydrazine, highlighting the octahedral-like structure, whereby the hydrazine occupies two octahedral sites (one for each nitrogen). Oxygen, nitrogen, and hydrogen atoms are colored red, blue and white, respectively, while Ni^{2+} is colored tan.

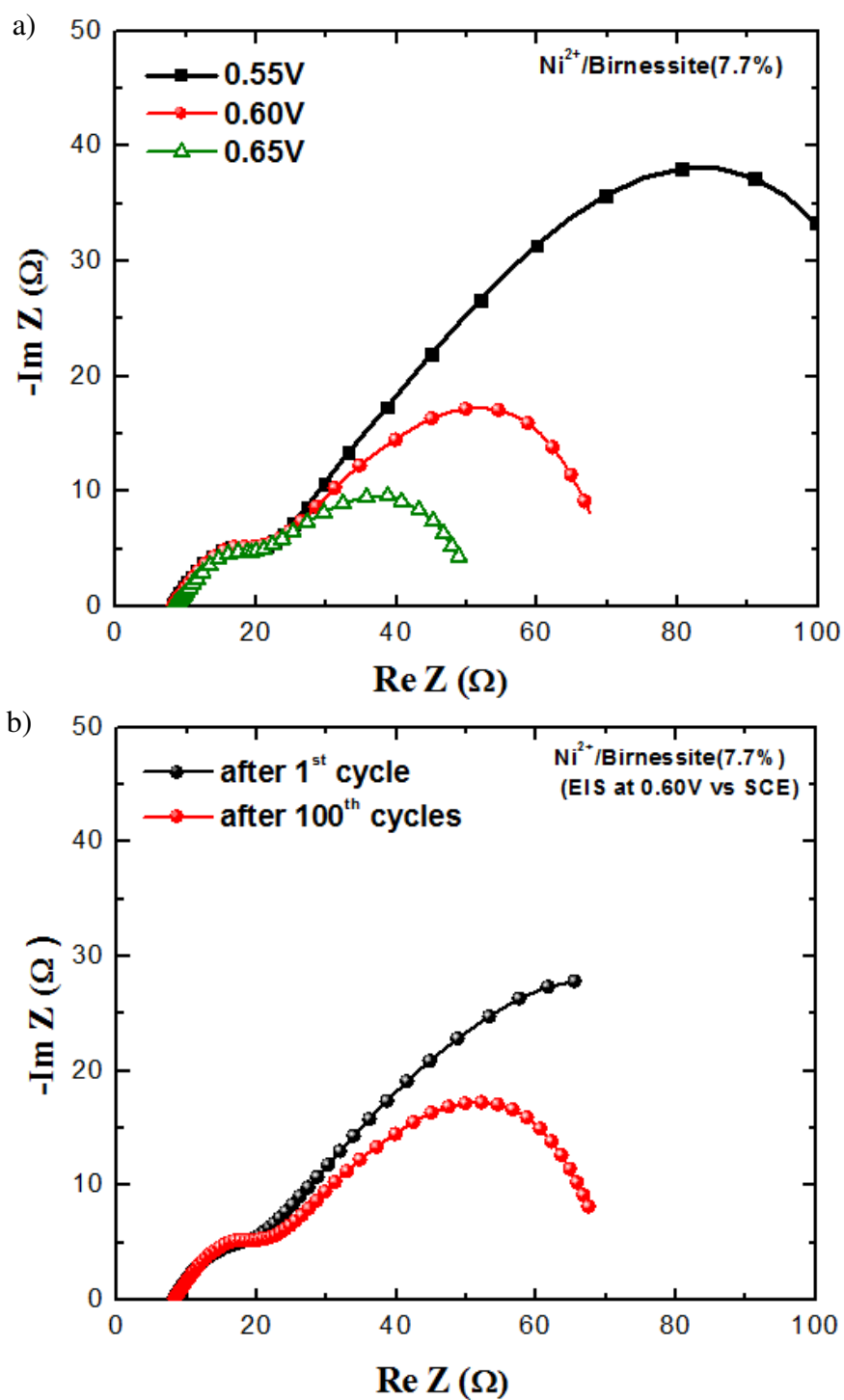


Figure S10. Nyquist plot obtained from EIS measurement: a) $\text{Ni}^{2+}/\text{birnessite}$ after 100 electrochemical cycles at an applied potential of 0.55V to 0.65V to (vs SCE) b) $\text{Ni}^{2+}/\text{birnessite}$ with increasing electrochemical cycles at 0.60 V (vs SCE).

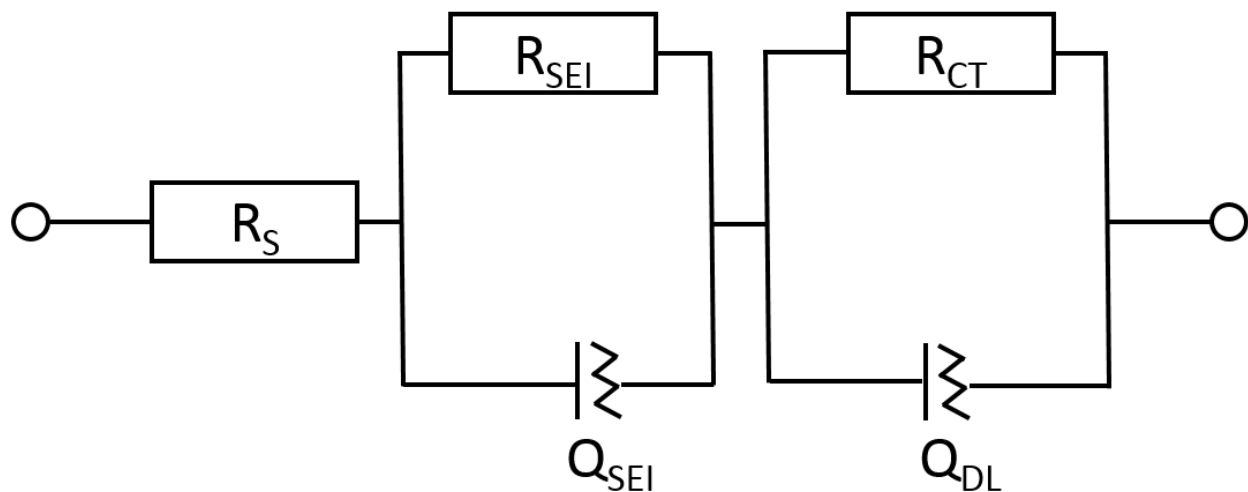


Figure S11. Equivalent circuit used to obtain charge transfer resistance of the OER catalysts

Where,

R_S - resistance of the electrolyte.

R_{SEI} - solid-electrolyte interphase resistance

Q_{SEI} - solid-electrolyte interphase capacitance (capacitance replaced by constant phase element (CPE) in order to account for non-ideality)

Q_{DL} - double layer capacitance (capacitance replaced by CPE in order to account for non-ideality)

R_{CT} - charge transfer resistance

Table S1. Parameters for fitted EIS spectra.

Catalyst	R_s/Ω	R_{SEI}/Ω	$Q_{SEI}/\mu F$	R_{ct}/Ω	$Q_{ct}/\mu F$
Ni ²⁺ /Birnessite at 0.55V after 100 cycles	9.0	15.0	128	102.0	553
Ni ²⁺ /Birnessite at 0.60V after 100 cycles	9.0	15.0	127	48.0	757
Ni ²⁺ /Birnessite at 0.65V after 100 cycles	9.0	15.0	130	27.0	951
Ni ²⁺ /Birnessite at 0.60V after 1st cycle	9.0	14.0	128	95.0	648

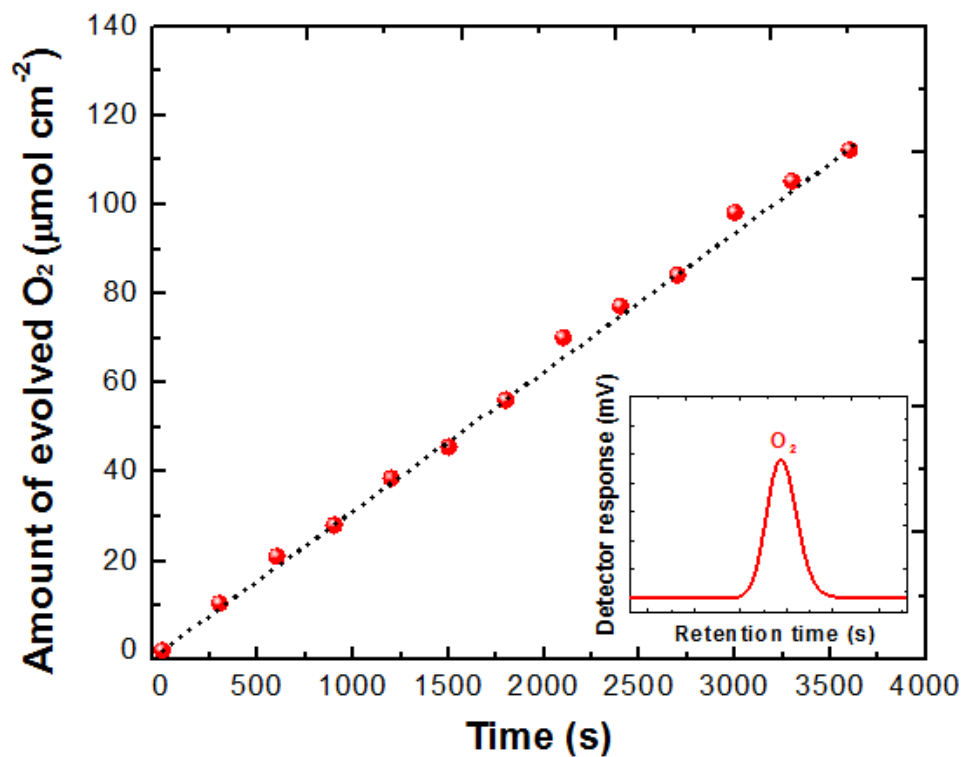


Figure S12. O₂ evolution from Ni²⁺/birnessite as a function of electrolysis time at constant current density 12 mA cm⁻². Inset is the obtained detector response (from GC) for evolved oxygen.

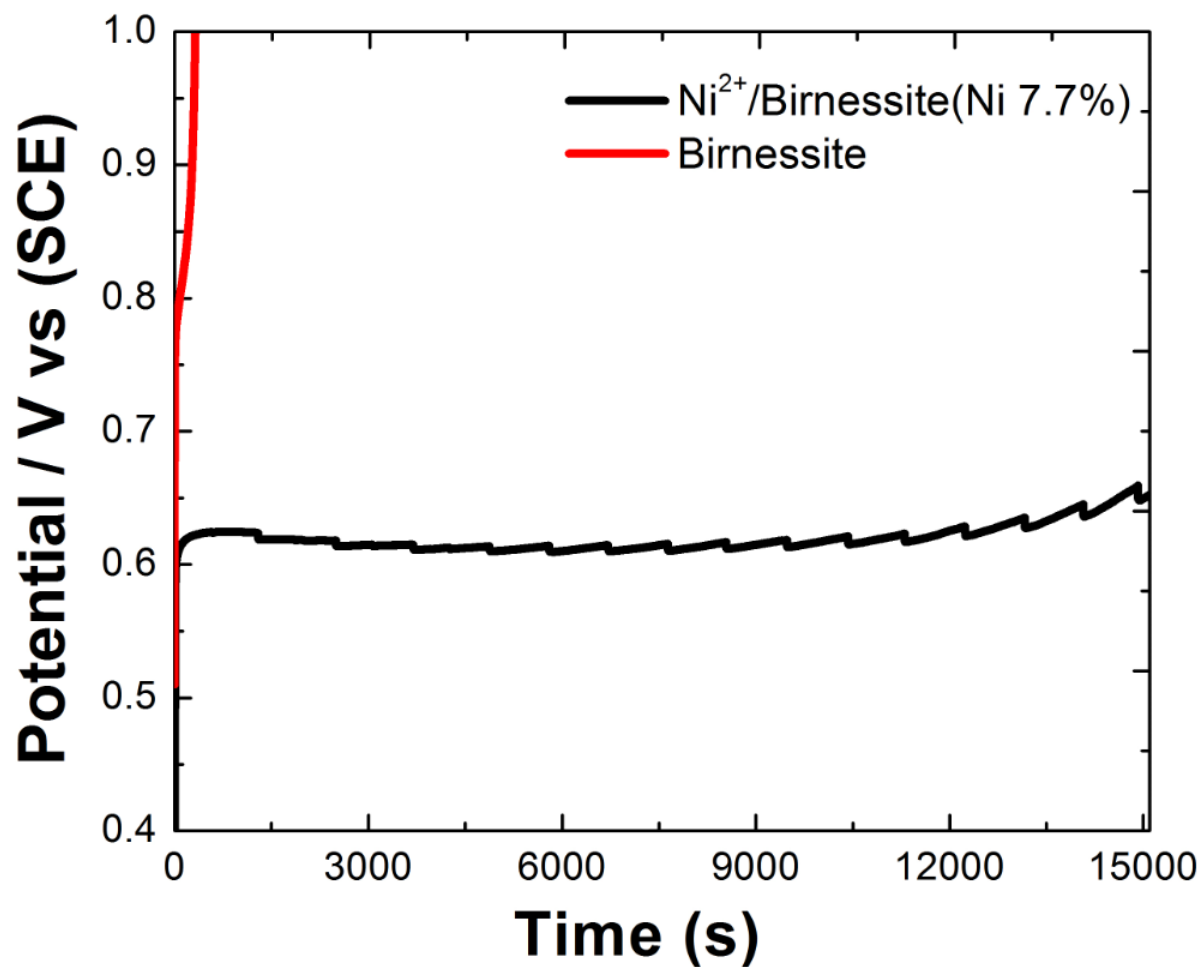


Figure S13. Chronopotentiometry curves for birnessite and Ni²⁺/birnessite at current densities of 5 mA cm⁻².

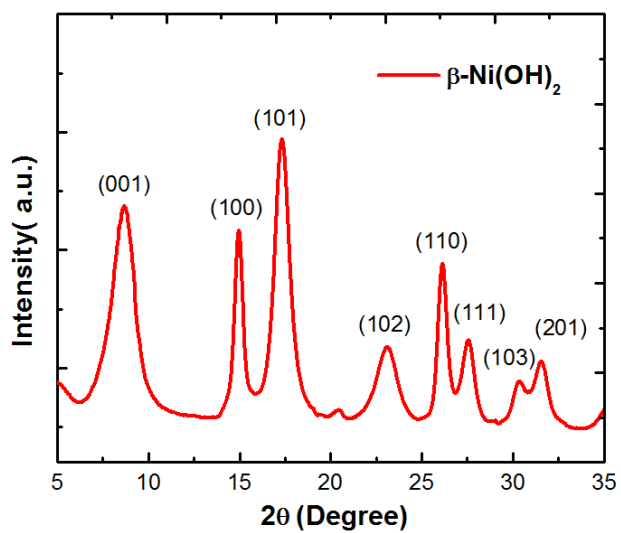


Figure S14. XRD spectra of β -nickel hydroxide.

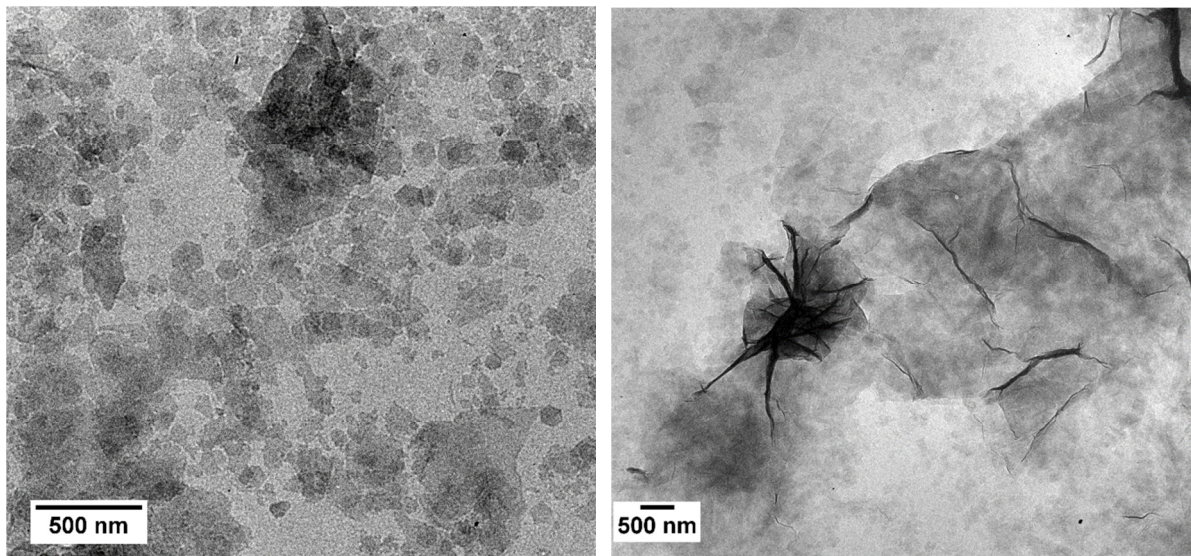


Figure S15. TEM images of β -nickel hydroxide.

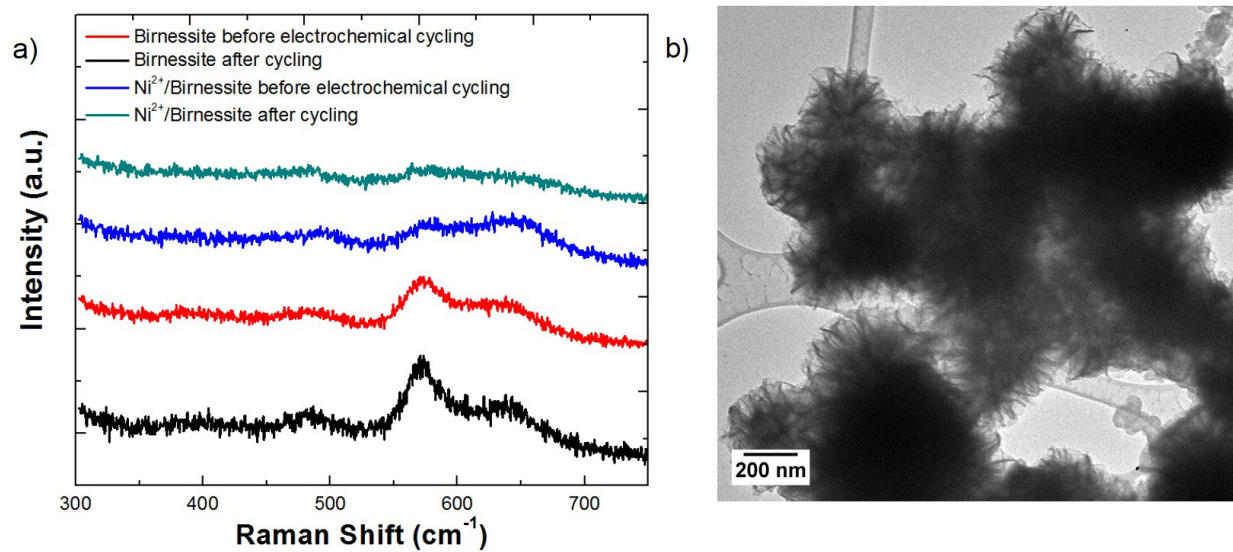


Figure S16. Raman spectra and TEM collected for catalyst ink. Raman spectra collected before and after electrochemical cycling of birnessite and Ni²⁺/birnessite. b) TEM micrograph of Ni²⁺/birnessite after electrochemical cycling. The Raman peaks are broadened in both birnessite and Ni²⁺/birnessite after electrochemical cycling, suggesting structural changes.

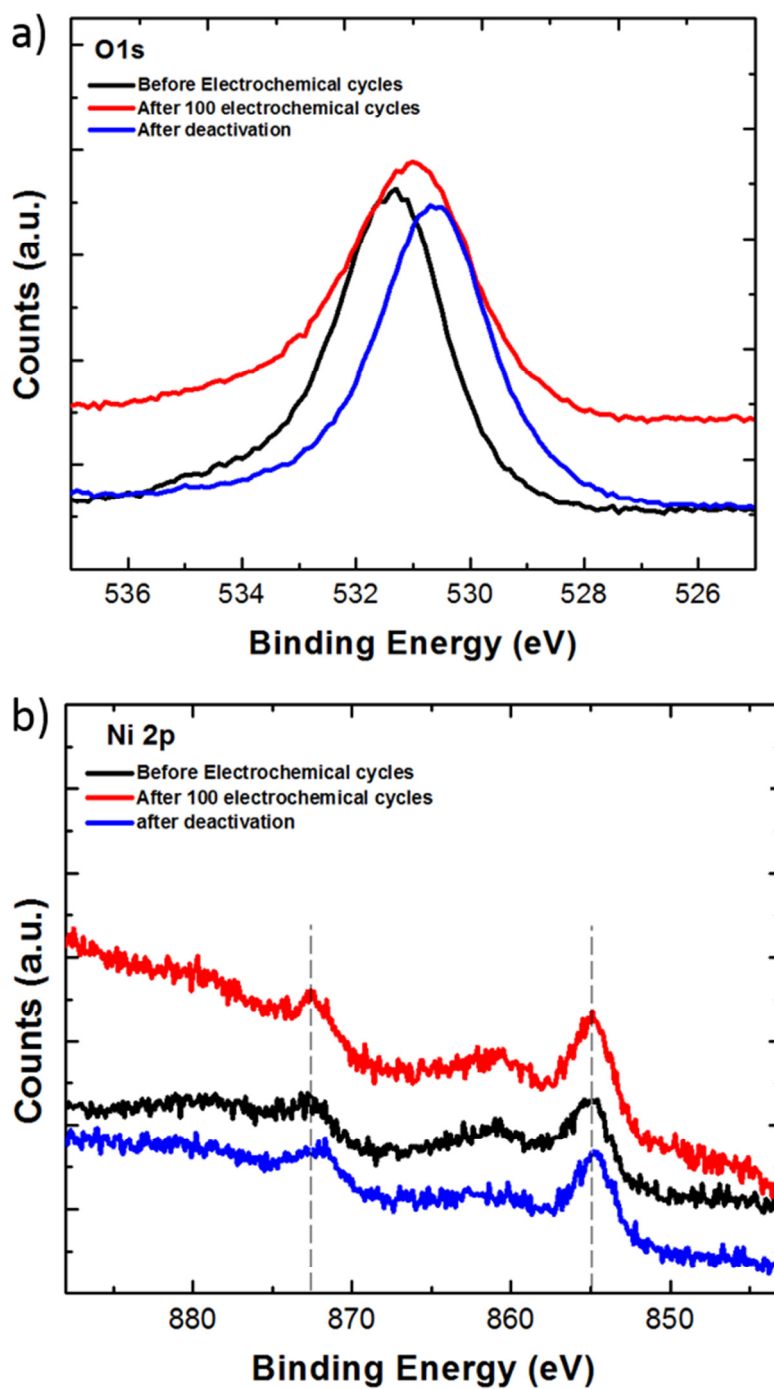


Figure S17. XPS of Ni²⁺/birnessite before and after electrochemical cycling: a) O 1s region, b) Ni 2p region. XPS spectra suggests that intercalated nickel in the birnessite interlayer undergoes an electrochemically induced phase transformation from Ni-hydroxide to Ni-oxide, which is based on the binding energy shift of the O 1s peak towards lower binding energy.

Table S2. Comparison of catalytic performance of Ni²⁺/MnO₂ to reported metal oxides catalysts.

Catalyst	Overpotential (10 mA cm⁻²)	Electrolyte	Tafel slope(mV/dec)	Reference
CoO_x	410	Phosphate buffer	60	15
Na₂CoP₂O₇	560	Phosphate buffer	80	16
MnO_x	-	Phosphate buffer	70	17
IrO₂	470	0.1M KOH	-	18
IrO₂	427	1M KOH	50	19
IrO₂	338	1M KOH	47	20
IrO₂	355	1M KOH	79	21
NiCo-Bulk	385	1M KOH	65	20
NiCo- nanosheets	334	1M KOH	41	20
LiCoO₂	430	1M KOH	48	22
α-MnO₂	480	0.1 KOH	77.5	23
Ni²⁺/MnO₂	400	1M KOH	60	This work

Capacitance measurements to estimate electrochemically active surface area (ECSA).

Estimation of the electrochemically active surface area (ECSA) of the catalysts was carried out by plotting charging current density differences ($\Delta j = j_a - j_c$) as a function of scan rate.^{20,24} The charging current density differences can be obtained by performing cyclic voltammetry (CV) at different scan rates in a potential window of 100 mV, where the open circuit potential (OCP) falls in the middle. The double layer capacitance can be estimated from the slope of charging current density differences at OCP vs scan rate, where the slope is twice the double layer capacitance. As double layer capacitance is proportional to the ECSA of the catalyst ratio of double layer capacitance can be considered as the ratio of the ECSA.^{20,24}

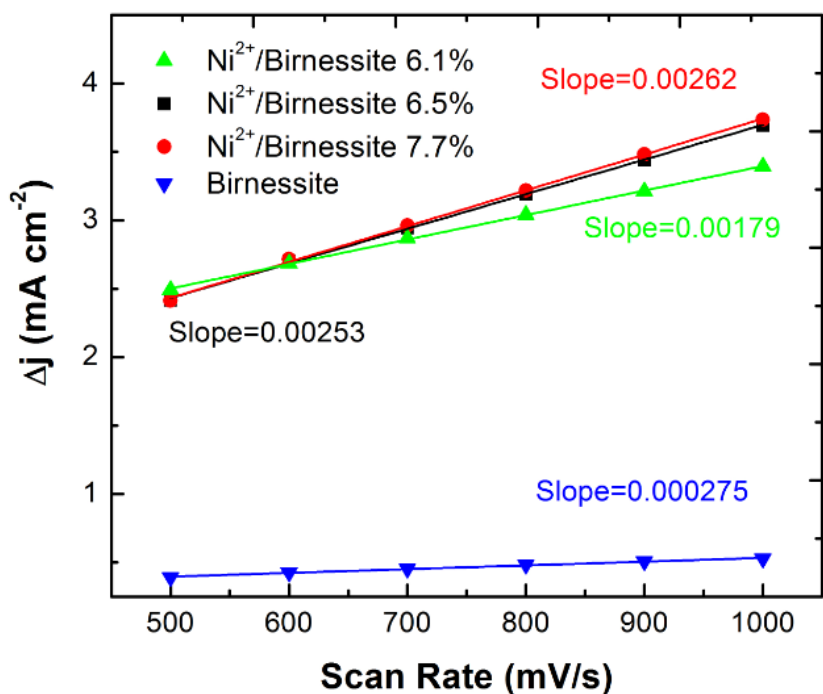


Figure S18. The difference in current density ($\Delta j = j_a - j_c$) at open circuit potential (OCP) plotted against scan rate fitted to a linear regression to estimate the ECSA of birnessite and Ni²⁺/Birnessite. The Ni²⁺/Birnessite shows a one order of magnitude higher ECSA than Birnessite suggesting Ni intercalation increases catalytic active sites for water oxidation.

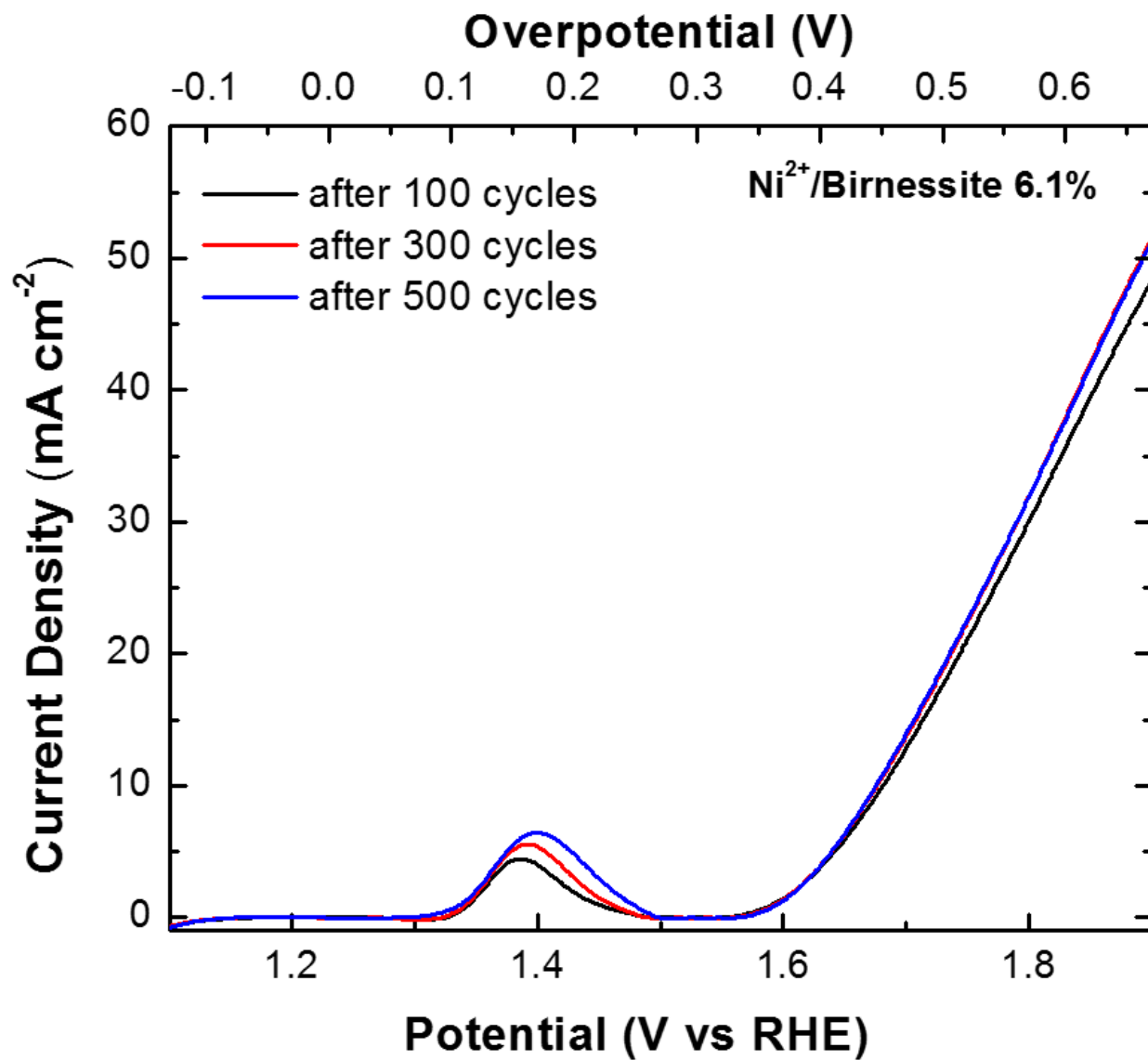


Figure S19. Polarization curves obtained after a specified number of electrochemical cycles for Ni^{2+} /Birnessite.

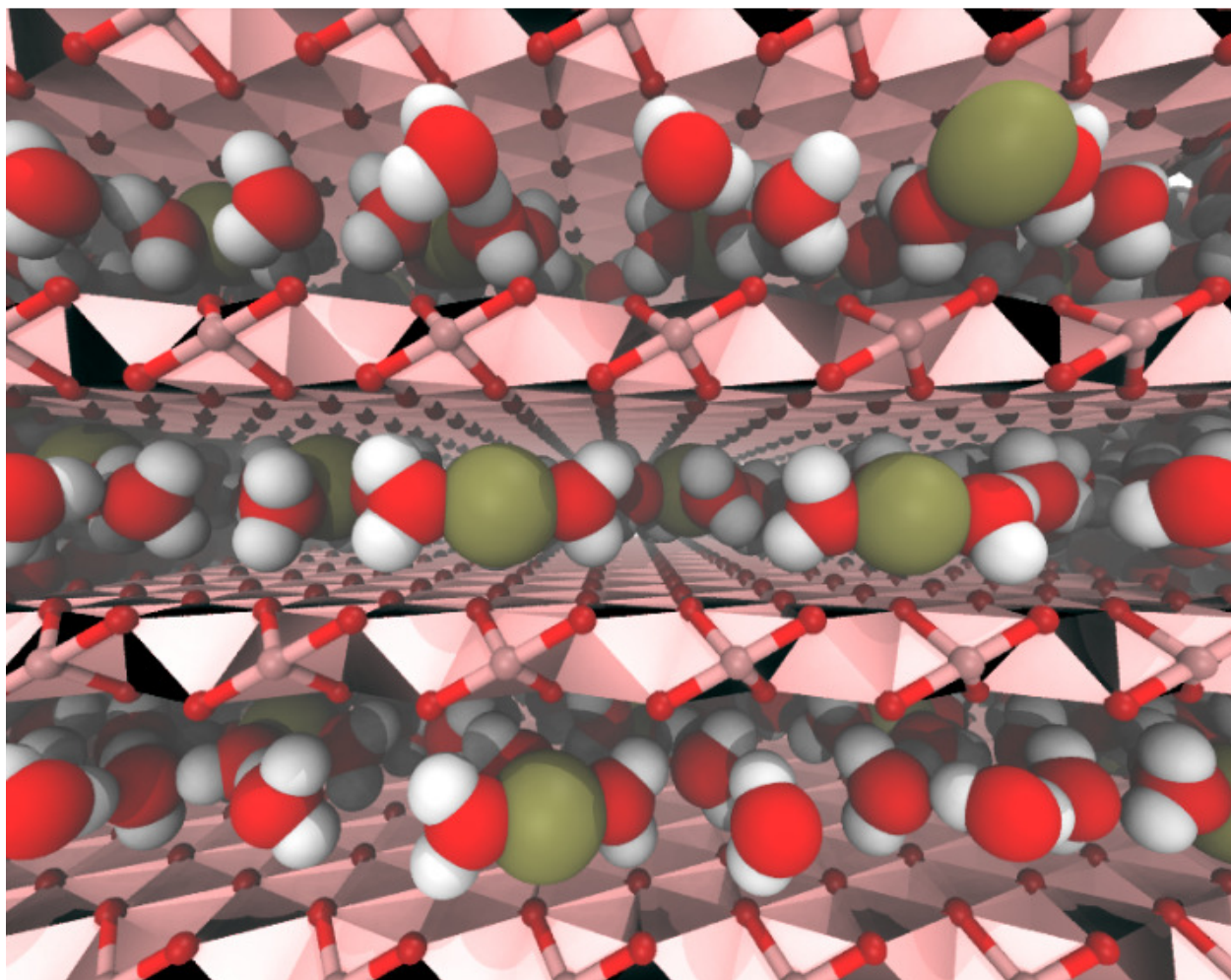


Figure S20. Microscopic picture of the Ni²⁺ ion intercalated birnessite used in MD simulations. Oxygen is colored in red, hydrogen is white, Mn is pink and Ni²⁺ is tan.

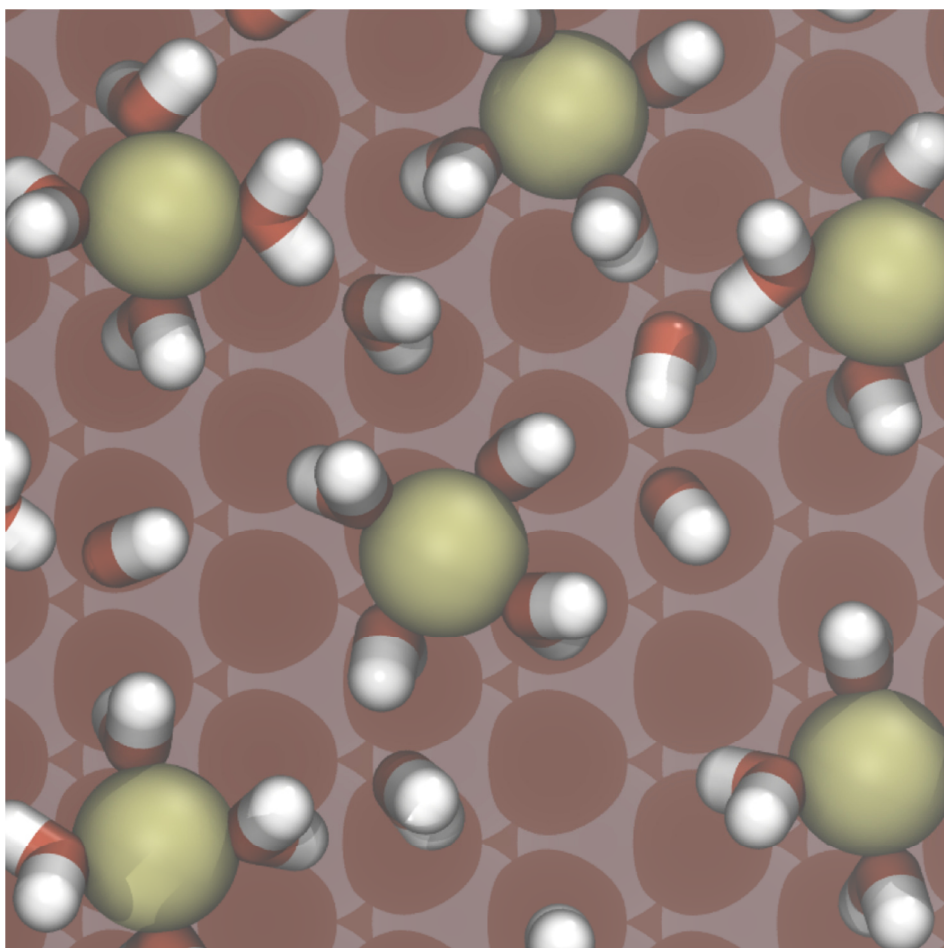


Figure S21. Snapshots of water and ions in Ni^{2+} /birnessite highlighting the orientational ordering of water and the octahedral coordination of Ni^{2+} (4 waters and 2 birnessite oxygens). Oxygens are colored red, manganese is pink, hydrogen atoms are white, and nickel ions are colored tan. Atoms of MnO_2 are rendered darker to highlight the ion hydration structure.

References

- 1 Nicholls, D. & Swindells, R. Hydrazine complexes of nickel(II) chloride. *Journal of Inorganic and Nuclear Chemistry* **30**, 2211-2217, doi:[http://dx.doi.org/10.1016/0022-1902\(68\)80219-2](http://dx.doi.org/10.1016/0022-1902(68)80219-2) (1968).
- 2 Remsing, R. C., McKendry, I. G., Strongin, D. R., Klein, M. L. & Zdilla, M. J. Frustrated Solvation Structures Can Enhance Electron Transfer Rates. *The Journal of Physical Chemistry Letters* **6**, 4804-4808, doi:10.1021/acs.jpcllett.5b02277 (2015).
- 3 Hess, B., Kutzner, C., van der Spoel, D. & Lindahl, E. GROMACS 4: Algorithms for Highly Efficient, Load-Balanced, and Scalable Molecular Simulation. *J. Chem. Theory Comp.*, 435 - 447 (2008).
- 4 Cygan, R. T., Liang, J.-J. & Kalinichev, A. G. Molecular Models of Hydroxide, Oxyhydroxide, and Clay Phases and the Development of a General Force Field. *J. Phys. Chem. B* **108**, 1255--1266 (2004).
- 5 Marcus, R. A. Electron Transfer Reactions in Chemistry. Theory and Experiment. *Rev. Mod. Phys.* **65**, 599--610 (1993).
- 6 Blumberger, J., Tavernelli, I., Klein, M. L. & Sprik, M. Diabatic Free Energy Curves and Coordination Fluctuations for the Aqueous $\text{Ag}^+/\text{Ag}^{2+}$ Redox Couple: a Biased Born-Oppenheimer Molecular Dynamics Investigation. *J. Chem. Phys.* **124**, 64507, doi:10.1063/1.2162881 (2006).
- 7 Ayala, R. & Sprik, M. A Classical Point Charge Model Study of System Size Dependence of Oxidation and Reorganization Free Energies in Aqueous Solution. *J. Phys. Chem. B* **112**, 257--269 (2008).
- 8 Li, P., Roberts, B. P., Chakravorty, D. K. & K. M. Merz, J. Rational Design of Particle Mesh Ewald Compatible Lennard-Jones Parameters for +2 Metal Cations in Explicit Solvent. *J. Chem. Theor. Comput.* **9**, 2733--2748 (2013).
- 9 Berendsen, H. J. C., Grigera, J. R. & Straatsma, T. P. The Missing Term in Effective Pair Potentials. *J. Phys. Chem.* **91**, 6269--6271 (1987).
- 10 Cygan, R. T., Post, J. E., Heaney, P. J. & Kubicki, J. D. Molecular Models of Birnessite and Related Hydrated Layered Minerals. *American Mineralogist* **97**, 1505--1514 (2012).
- 11 Gutowski, K. E., Gurkan, B. & Maginn, E. J. Force field for the atomistic simulation of the properties of hydrazine, organize hydrazine derivatives, and energetic hydrazinium ionic liquids. *Pure Appl. Chem.* **81**, 1799--1828 (2009).
- 12 Bussi, G., Donadio, D. & Parrinello, M. Canonical Sampling Through Velocity Rescaling. *J. Chem. Phys.* **126**, 014101 (2007).
- 13 Bussi, G., Timan, T. & Parrinello, M. Isothermal-isobaric molecular dynamics using stochastic velocity rescaling. *The Journal of Chemical Physics* **130**, 074101, doi:10.1063/1.3073889 (2009).
- 14 Duarte, F. *et al.* Force Field Independent Metal Parameters Using a Nonbonded Dummy Model. *The Journal of Physical Chemistry B* **118**, 4351-4362, doi:10.1021/jp501737x (2014).
- 15 Gerken, J. B. *et al.* Electrochemical Water Oxidation with Cobalt-Based Electrocatalysts from pH 0–14: The Thermodynamic Basis for Catalyst Structure, Stability, and Activity. *Journal of the American Chemical Society* **133**, 14431-14442, doi:10.1021/ja205647m (2011).

- 16 Kim, H. *et al.* Coordination tuning of cobalt phosphates towards efficient water oxidation catalyst. *Nat Commun* **6**, doi:10.1038/ncomms9253 (2015).
- 17 Huynh, M., Shi, C., Billinge, S. J. L. & Nocera, D. G. Nature of Activated Manganese Oxide for Oxygen Evolution. *Journal of the American Chemical Society* **137**, 14887-14904, doi:10.1021/jacs.5b06382 (2015).
- 18 Lee, Y., Suntivich, J., May, K. J., Perry, E. E. & Shao-Horn, Y. Synthesis and Activities of Rutile IrO₂ and RuO₂ Nanoparticles for Oxygen Evolution in Acid and Alkaline Solutions. *The Journal of Physical Chemistry Letters* **3**, 399-404, doi:10.1021/jz2016507 (2012).
- 19 Trotochaud, L., Ranney, J. K., Williams, K. N. & Boettcher, S. W. Solution-Cast Metal Oxide Thin Film Electrocatalysts for Oxygen Evolution. *Journal of the American Chemical Society* **134**, 17253-17261, doi:10.1021/ja307507a (2012).
- 20 Song, F. & Hu, X. Exfoliation of layered double hydroxides for enhanced oxygen evolution catalysis. *Nat Commun* **5**, doi:10.1038/ncomms5477 (2014).
- 21 Yu, M. Q. *et al.* Mn₃O₄ nano-octahedrons on Ni foam as an efficient three-dimensional oxygen evolution electrocatalyst. *Journal of Materials Chemistry A* **3**, 14101-14104, doi:10.1039/C5TA02988K (2015).
- 22 Gardner, G. *et al.* Structural basis for differing electrocatalytic water oxidation by the cubic, layered and spinel forms of lithium cobalt oxides. *Energy & Environmental Science* **9**, 184-192, doi:10.1039/C5EE02195B (2016).
- 23 Meng, Y. *et al.* Structure–Property Relationship of Bifunctional MnO₂ Nanostructures: Highly Efficient, Ultra-Stable Electrochemical Water Oxidation and Oxygen Reduction Reaction Catalysts Identified in Alkaline Media. *Journal of the American Chemical Society* **136**, 11452-11464, doi:10.1021/ja505186m (2014).
- 24 Xie, J. *et al.* Atomically-thin molybdenum nitride nanosheets with exposed active surface sites for efficient hydrogen evolution. *Chemical Science* **5**, 4615-4620, doi:10.1039/C4SC02019G (2014).